Scientific Research Publishing

Open Journal of Microphysics, 2026, 16(1), 1-19
https://www.scirp.org/journal/ojm
ISSN Online: 2162-2469
ISSN Print: 2162-2450

Elastic Stability and Multifunctional Properties of Wurtzite Aluminum Nitride from First Principles

Mobisa Kemuma Deborah*, Calford Odhiambo Otieno, Ketui Daniel, Otieno Ochieng Victor

Department of Physics, Kisii University, Kisii, Kenya
Email: *deborahmobisa@gmail.com, cotieno@kisiiuniversity.ac.ke, dketui@kisiiuniversity.ac.ke, victorothevictor@gmail.com

How to cite this paper: Deborah, M.K., Otieno, C.O., Daniel, K. and Victor, O.O. (2026) Elastic Stability and Multifunctional Properties of Wurtzite Aluminum Nitride from First Principles. *Open Journal of Microphysics*, **16**, 1-19.
https://doi.org/10.4236/ojm.2026.161001

Received: February 1, 2026
Accepted: February 25, 2026
Published: February 28, 2026

Abstract

Elastic stability is a critical requirement for piezoelectric materials intended for reliable energy-harvesting operation under cyclic mechanical and thermal loading. In this work, we present a convergence-verified first-principles density-functional theory (DFT) investigation of the elastic stability and multifunctional properties of wurtzite aluminum nitride (AlN). Structural optimization yields equilibrium lattice parameters of a = 3.111 Å and c = 4.978 Å. The calculated elastic constants satisfy all Born stability criteria for hexagonal crystals, confirming the mechanical stability of wurtzite AlN. Voigt-Reuss-Hill averaging reveals high bulk, shear and Young's moduli together with pronounced elastic anisotropy. The calculated elastic moduli indicate a stiff material with brittle mechanical character. Electronic band-structure and density-of-states analyses confirm a wide direct Γ-Γ band gap, consistent with ultra-wide-band-gap nitride behavior and high electrical insulation. Thermoelectric transport trends, evaluated within the constant relaxation time approximation, show moderate Seebeck coefficients but very low electrical conductivity and high lattice thermal conductivity, resulting in poor intrinsic thermoelectric efficiency. These results establish a consistent theoretical benchmark linking elastic stability, electronic structure and transport behavior in wurtzite AlN and clarify its suitability as a robust, lead-free material platform for piezoelectric energy-harvesting applications.

Keywords

Wurtzite Aluminum Nitride, Elastic Stability, First-Principles Calculations, Density-Functional Theory, Elastic Anisotropy, Electronic Band Structure, Thermoelectric Transport, Piezoelectric Energy Harvesting

1. Introduction

Aluminium nitride (AlN) is a technologically significant nitride and a wide-band-gap semiconductor whose exceptional thermal, mechanical and electrical properties have enabled its wide-spread adoption in high-power electronics, acoustic resonators, optoelectronic devices and microelectromechanical systems (MEMS). Its wurtzite crystal structure of space group $P6_3mc$ exhibits strong ionic-covalent bonding, high thermal conductivity and sustained structural integrity at temperatures exceeding 1300˚C, making it attractive for extreme-environment applications. These features, together with a direct band gap of 6.2 eV, low dielectric permittivity and a moderate piezoelectric coefficient (d_{33} = 5.5 pm·V^{-1}), position AlN as a leading candidate for next-generation energy-harvesting and electromechanical technologies.

Despite its extensive use in thin-film resonators and high-frequency filters, comparatively less attention has been given to understanding how AlN's intrinsic mechanical properties, such as its elastic constants, stiffness, ductility index and mechanical stability criteria, fundamentally govern its reliability and performance in advanced device platforms. Most existing studies emphasize synthesis, thermal conductivity or optical behavior, leaving a critical gap in high-accuracy, first-principles datasets for mechanical behavior particularly those obtained through convergence tested density functional theory (DFT) calculations.

A clear understanding of the intrinsic mechanical response of wurtzite AlN is required because elastic stiffness, dielectric behavior and structural anisotropy collectively govern its electromechanical performance. In particular, the characteristically low dielectric permittivity of AlN must be preserved to maintain acoustic-resonator efficiency. Therefore, a rigorous first-principles evaluation of the elastic properties provides the microscopic basis for predicting material reliability and for guiding alloying or doping strategies.

In this study, we perform a systematic, convergence-verified first-principles (DFT) investigation of the structural and mechanical properties of wurtzite AlN. We compute its elastic constants, Voigt-Reuss-Hill averaged moduli, Pugh's ratio and mechanical stability criteria and link these descriptors to its electronic structure to establish a self-consistent picture of its intrinsic behavior. The findings offer a reliable theoretical baseline for future work on AlN-based piezoelectric, electromechanical and energy-harvesting devices, as well as for the rational design of AlN alloys and hetero structures. Its hexagonal structure is defined by a = b ≠ c and $\alpha = \beta = 90^\circ$, $\gamma = 120^\circ$. Two other phases are known: a zinc-blende polymorph (metastable, $F\bar{4}3m$), which can exhibit piezoelectricity that is typically much weaker than wurtzite and a rock-salt polymorph which is centrosymmetric that forms only under high pressure and is non-piezoelectric [1].

While numerous DFT studies of AlN exist, they often focus on isolated property domains; electronic, mechanical or thermal, without rigorous convergence testing or cross-property integration. The present work addresses this limitation by implementing a unified, convergence-validated DFT framework that consistently

correlates structural, electronic, mechanical and thermoelectric descriptors within a single computational protocol. Numerical parameters, including plane-wave cutoff energy and k-point density, are systematically tested to ensure the reliability of all reported quantities. This integrated approach enables a direct linkage between intrinsic material properties and their implications for electromechanical performance. Figure 1 illustrates the conventional unit cell and a 2 × 2 × 2 supercell of the wurtzite structure as obtained from the burai

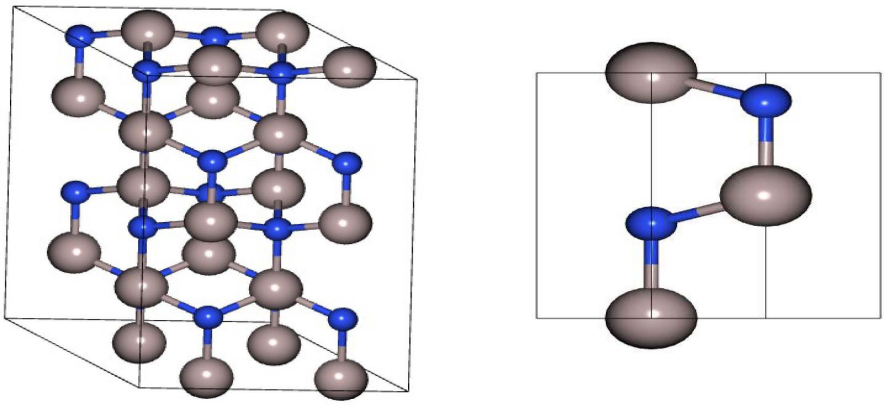

Figure 1. The conventional unit cell and a 2 × 2 × 2 supercell of the wurtzite structure.

Complementing its structural and thermal merits, AlN exhibits a wide, direct band gap of about 6.2 eV [2]. Owing to its non-centrosymmetric wurtzite crystal structure, it also shows pronounced piezoelectric behavior and a significant second-order nonlinear optical response (χ^2 = 4.7 pm·V^{-1}) [3]. These properties underpin its application in optoelectronic and electromechanical devices and have motivated efforts to optimize its performance through compositional and microstructural control. Such optimization, however, requires reliable knowledge of the intrinsic structural, elastic, and electronic properties that can be systematically obtained from first-principles calculations. Consequently, AlN is widely employed in high-frequency resonators, filters, and MEMS-based energy-harvesting systems [2].

2. Methodology

The workflow began by retrieving the AlN crystal structure from the Crystallography Open Database via a compound-name query [4]. This open repository provides Crystallographic Information Files (CIFs) containing lattice parameters, space-group symmetry and atomic coordinates, which served as the starting point for our simulations. The CIF was then imported into Burai, a graphical front-end for Quantum ESPRESSO that supports CIF ingestion, visualization and automatic generation of QE-compatible input files [5]. The first-principles calculations were performed using density-functional theory as implemented in *Quantum ESPRESSO*. The exchange-correlation interaction was treated within the generalized gradient approximation using the Perdew-Burke-Ernzerhof (PBE) functional. Core-va-

lence interactions were described using PBE projector-augmented-wave pseudopotentials from the SSSP library, with Al ($3s^2 3p^1$) and N ($2s^2 2p^3$) treated as valence states and no semicore states included. The plane-wave kinetic-energy cutoff was 70 Ry with a charge-density cutoff of 560 Ry. Brillouin-zone integrations employed a Monkhorst-Pack k-point mesh of 12 × 12 × 8 for self-consistent calculations and denser meshes for DOS. Structural relaxation was carried out using the BFGS algorithm until forces were below 10^{-3} Ry/Bohr and total-energy changes below 10^{-4} Ry. Gaussian smearing of 0.01 Ry was applied only to aid convergence. No van der Waals correction and no spin-orbit coupling were included. From the COD structure wurtzite AlN of space group $P6_3mc$, Structural optimization and bulk-property calculations were performed using the primitive wurtzite unit cell (space group $P6_3mc$). The optimized lattice parameters were a = 3.111 Å and c = 4.978 Å (c/a = 1.600), with an internal structural parameter u = 0.382. The relaxed fractional atomic coordinates were Al at (0, 0, 0) and (2/3, 1/3, 1/2), and N at (0, 0, u) and (2/3, 1/3, 1/2 + u). The primitive cell was sufficient for structural, electronic and elastic calculations because these are bulk periodic properties, while a 2 × 2 × 2 supercell was used only for visualization and post-processing analyses to improve graphical representation and avoid Brillouin-zone folding effects.

Subsequent structural optimization was performed by specifying the plane-wave cutoffs, Monkhorst-Pack k-point meshes and appropriate pseudopotentials within QE, with convergence criteria set to ensure reliable total energies and relaxed geometries.

The input files were then transferred to a high-performance computing (HPC) cluster via secure file transfer (WinSCP) and output data were retrieved similarly. Remote job submission and monitoring were performed over an SSH terminal (PuTTY). Quantum ESPRESSO calculations were launched by submitting batch scripts to the cluster's job scheduler and run status was tracked in real time via scheduler queues and log files.

The novelty of our computational approach lies in its systematic validation across multiple property domains. Unlike studies that adopt generic parameters, we performed separate convergence tests for structural, electronic, mechanical and thermoelectric analyses, ensuring each property is computed with optimal numerical settings. This multi-property convergence strategy minimizes transfer errors and provides a self-consistent dataset suitable for cross-property correlations essential for energy harvesting material design.

3. Results and Discussion

The convergence of the total energy with respect to the plane-wave kinetic-energy cutoff (ecut) is shown in **Figure 2**. Beyond 70 Ry, the total energy variation is less than 10^{-3} Ry per atom, while computational cost remains reasonable. We therefore adopted 70 Ry as the planewave kinetic-energy cutoff for all subsequent calculations (with a charge-density cutoff ecutrho = 560 Ry, *i.e.*, 8× ecut), ensuring well-converged energies for the reported properties. We increased the mesh den-

sity until key quantities total energy, charge density and band-structure features became insensitive to further refinement. On this basis, we adopt a 12 × 12 × 8 k-point grid for all production self-consistent field (SCF) calculations. This kept total-energy changes below 10^{-3} Ry/atom and provided sufficient accuracy for forces, elastic constants and anisotropic properties (a denser non-SCF mesh was used for DOS calculations as noted).

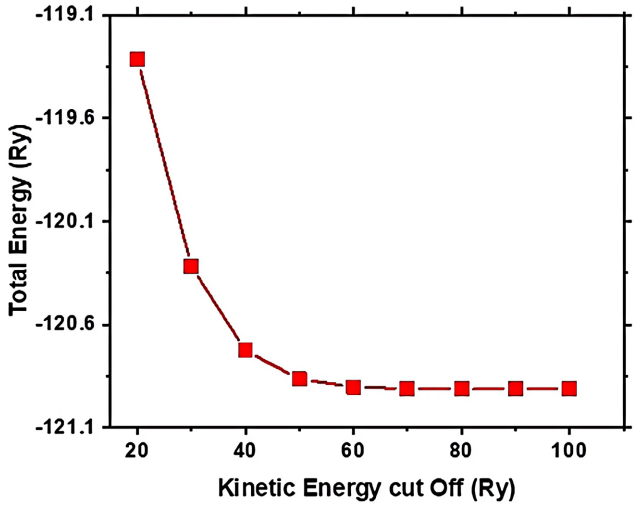

Figure 2. Convergence of total energy with plane-wave cutoff.

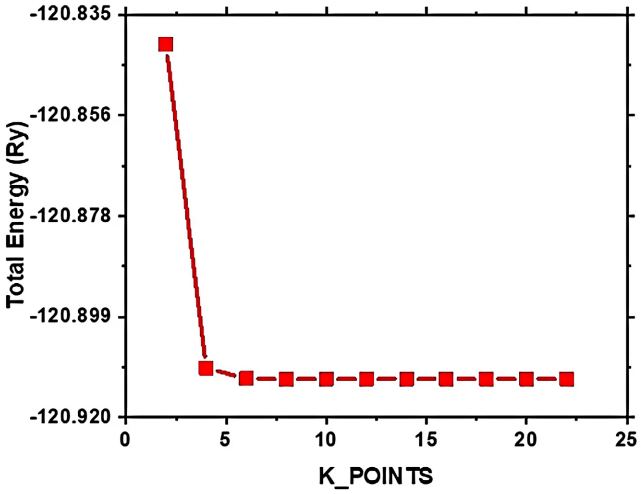

Figure 3. Variation of total energy with k-point.

As shown in Figure 3, the total energy decreases rapidly with increasing k-point density and becomes effectively converged beyond a 6 × 6 × 6 Monkhorst-Pack grid, after which further refinement leads to negligible energy variations. To provide additional numerical robustness for the calculation of forces, stresses, elastic constants, and anisotropic response properties, a denser 12 × 12 × 8 Monkhorst-Pack mesh was employed for all production self-consistent-field (SCF) calculations. The anisotropic sampling reflects the hexagonal symmetry of the AlN crys-

tal structure. With this mesh, the variation in total energy was reduced to below 10^{-4} Ry per atom, ensuring well-converged structural and mechanical properties while maintaining reasonable computational cost. For electronic density-of-states (DOS) calculations, a further refined non-self-consistent (NSCF) k-point mesh was used where indicated.

The equilibrium lattice parameters were obtained by scanning the total-energy surface E(a, c), as shown in Figure 4 and relaxing internal coordinates at each trial cell geometry. The energy strain curves show the expected behavior: both compressive and tensile deviations raise the total energy, with a clear minimum at a = 3.111 Å (in-plane lattice constant) and c = 4.978 Å (lattice constant along c-axis). These optimized lattice constants define the most stable wurtzite-AlN configuration; moving away from them increases E, confirming the reliability of our structural optimization.

To determine the equilibrium a and c of wurtzite AlN, we performed a series of total-energy calculations on unit cells whose volumes were uniformly scaled about an initial guess. At each trial volume, the internal coordinates (and the c/a ratio for wurtzite) were relaxed under the space-group symmetry. The resulting energy versus data were then fitted to the third-order Birch-Murnaghan.

The optimized a and c values were obtained by fitting the calculated total energies to the Birch-Murnaghan equation and then solving for the parameters that minimize the internal stress. These parameters play a vital role for evaluating the mechanical stability of the material when subjected to stress especially when it is intended for energy harvesting by determining the equilibrium volume bulk modulus and compressibility of AlN and its doped variants.

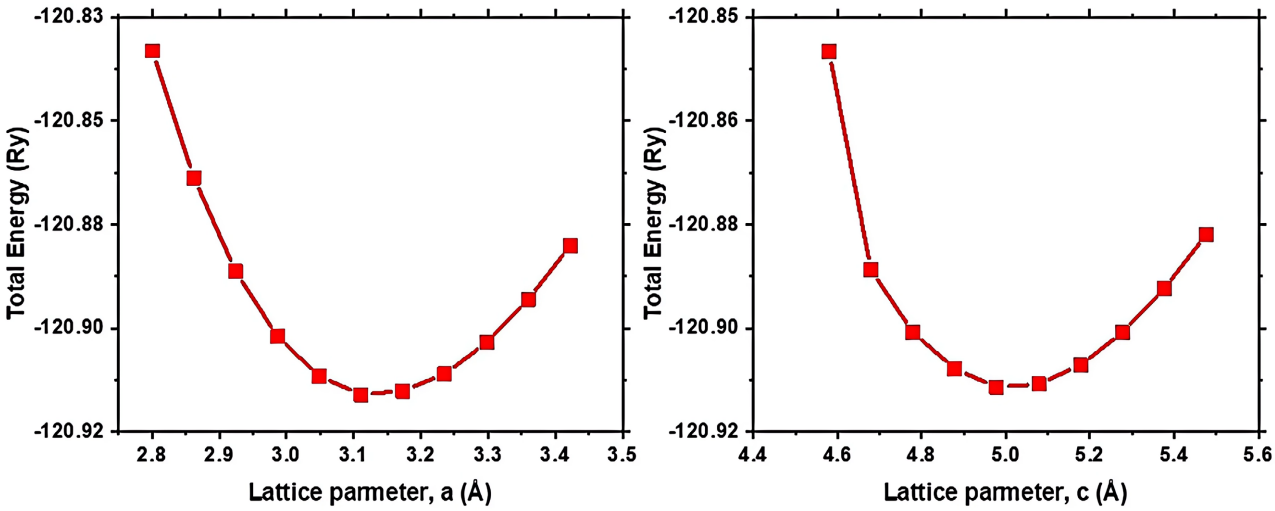

Figure 4. (a): Variation of total energy with lattice parameter a (Å) & (b): Variation of total energy with lattice parameter c (Å).

3.1. Electronic Properties

The electronic band structure and projected density of states (PDOS) of AlN were

calculated to elucidate its fundamental electronic behavior (**Figure 5(a)** and **Figure 5(b)**). As shown in the band structure (**Figure 5(a)**), the valence-band maximum (VBM) is located at the Γ point and the conduction-band minimum (CBM) also occurs at the same k-point, indicating that AlN exhibits a direct band gap (Γ-Γ transition). The identification of a direct band gap is based on the coincidence of the highest occupied and lowest unoccupied electronic states at the Brillouin-zone center. This result is consistent with recent experimental measurements and advanced first-principles calculations, which report wurtzite AlN as a direct ultra-wide-band-gap semiconductor with the band edges located at Γ [6] [7].

Although the present calculations were performed using a semilocal exchange-correlation functional, which is known to underestimate the absolute magnitude of band gaps, the nature and k-space position of the band gap are reliably described. Recent quasiparticle GW studies and optical experiments place the direct band gap of AlN in the range of approximately 6.0 - 6.3 eV, confirming that the Γ-Γ transition remains unchanged across different theoretical formalisms [6] [7]. Therefore, while the computed gap value is expectedly smaller, the predicted electronic topology remains physically meaningful and consistent with modern literature.

Further insight into the electronic structure is obtained from the PDOS shown in **Figure 5(b)**. The upper valence band is dominated primarily by nitrogen 2p states, whereas the conduction-band edge is mainly composed of aluminum 3s and 3p orbitals. This orbital separation reflects the characteristic bonding nature of III-nitride compounds, where the valence band arises from anion p-state hybridization and the conduction band exhibits stronger cation character. Similar orbital distributions near the band edges have been reported in recent density-functional and k·p parameterization studies of AlN and related nitride alloys, confirming the reliability of the present electronic description [8] [9].

The coexistence of a direct band gap at Γ (**Figure 5(a)**) and a clear separation of valence and conduction-band orbital characters (**Figure 5(b)**) underpins the optical transparency of AlN in the visible region and its suitability for deep-ultraviolet optoelectronic applications. At the same time, the large band gap and low intrinsic carrier concentration impose intrinsic limitations on electrical conductivity,

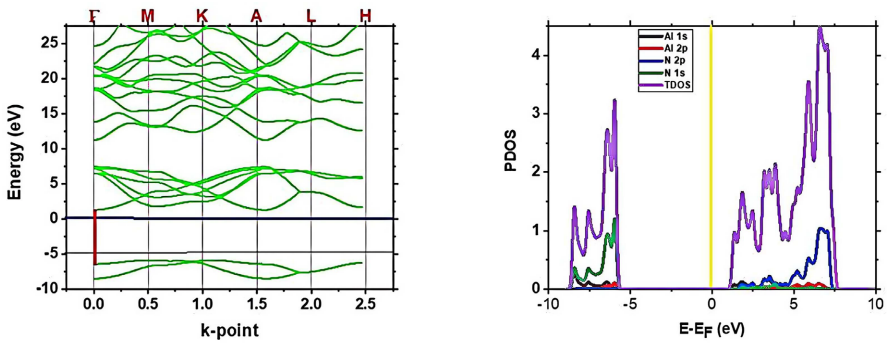

Figure 5. (a): Electronic band structure of wurtzite AlN; (b): Total and projected DOS for wurtzite AlN.

which is consistent with the generally weak thermoelectric performance observed in ultra-wide-band-gap nitrides. These electronic characteristics establish AlN as a reference material for high-power electronics, deep-UV photonics, and nitride-based heterostructure engineering [9].

3.2. Mechanical Properties

The elastic constants were determined using the finite-strain energy method. Symmetry-adapted homogeneous strains appropriate for hexagonal crystals were applied to the relaxed equilibrium structure, and internal atomic coordinates were fully relaxed for each strained configuration. Strain amplitudes of ±0.5%, ±1.0% and ±1.5% were used, providing multiple strain points for each deformation mode. The total energies were fitted to a quadratic strain-energy relation, and the elastic stiffness coefficients were obtained from the curvature of the fits; energies rather than stresses were used for improved numerical stability. The calculated elastic constants were C11 = 374 GPa, C12 = 127.97 GPa, C13 = 98.00 GPa, C33 = 392 GPa and C44 = 125 GPa, which satisfy the Born stability criteria for hexagonal crystals.

The mechanical response of wurtzite AlN is governed by its elastic stiffness tensor Cij, which describes the linear relationship between applied stress and the resulting strain [10]. These elastic constants provide the fundamental link between atomic bonding and macroscopic mechanical behavior, including resistance to volume change, shear deformation and uniaxial loading. Accurate determination of Cij is therefore essential for evaluating the suitability of AlN for energy-harvesting and electromechanical applications, where mechanical robustness and elastic anisotropy directly influence device performance [11].

The elastic constants were calculated using the first-principles energy-strain method [12]. In this approach, small symmetry-preserving homogeneous deformations are applied to the equilibrium wurtzite structure and the total energies of the strained configurations are computed after relaxing all internal atomic coordinates [12]. Because the total energy can be expanded to second order in the strain components, the curvature of the energy-strain relationships yields the elastic stiffness coefficients [13]. This method provides a self-consistent and accurate description of elastic properties, particularly for anisotropic hexagonal crystals [14].

Mechanical stability of hexagonal AlN was evaluated using the Born stability criteria, which require that specific combinations of elastic constants remain positive in order to ensure resistance against all symmetry-allowed lattice distortions [15]. These conditions guarantee that the crystal is mechanically stable under small deformations.

To determine the elastic constants in practice, five linearly independent homogeneous strain modes were applied: 1) an in-plane biaxial strain that changes the basal lattice parameter a while keeping c fixed; 2) a uniaxial strain along the c-axis at fixed a; 3) a volume-conserving orthorhombic in-plane strain used to isolate C11 − C12; 4) a shear strain $\varepsilon 4$ to obtain C44; and 5) a basal-plane shear strain $\varepsilon 6$ to obtain C66 [16]. Fitting the resulting energy-strain relations yields the inde-

pendent elastic constants consistent with hexagonal symmetry.

The elastic stiffness tensor was expressed in standard 6 × 6 Voigt notation [12]. For hexagonal AlN, only five elastic constants are independent: C11, C12, C13, C33, and C44, with C66 = (C11 − C12)/2 and C55 = C44 by symmetry [12]. The hydrostatic elastic response is described by the combination Czz = C11 + C12 +2C33 − 4C13 [17].

The resulting elastic constants fully characterize the stiffness, directional rigidity and shear resistance of wurtzite AlN and provide the basis for computing the bulk modulus, shear modulus, Young's modulus, and elastic anisotropy, which collectively govern its mechanical reliability and energy-harvesting performance. The calculated elastic constants satisfy the Born stability conditions for hexagonal crystals, as summarized in Table 1.

Table 1. Born stability criteria.

Condition	Expression	Results	Conclusion
Symmetry 1	$C11 > \lvert C12 \rvert$	374 > 127.97	Stable
Symmetry 2	$2(C13)^2 < C33(C11+C12)$	19321.85 < 178168.33	Stable
Symmetry 3	$(C11+C12)C33 > 2C_{13}^2$	191752.54 > 19208	Stable
Symmetry 4	C66 > 0 where C66 = (C11 − C12)/2	123.02 > 0	Stable

We obtained the bulk modulus (B), shear modulus (G), and Young's modulus (E) of polycrystalline AlN using Voigt-Reuss-Hill averaging. As expected, a larger E indicates a stiffer solid; literature trends show E for rock-salt > E for wurtzite > E for zinc-blende (noting that rock-salt is a high-pressure, non-piezoelectric phase).

Table 2 summarizes the computed bulk modulus, shear modulus, and Pugh's ratio from this study, and compares them to values from the existing literature.

Table 2. Computed bulk modulus, shear modulus, and Pugh's ratio for w-AlN, with percentage deviations from literature values.

Property	Averaging Scheme	Our values	Experiment values	% difference
Bulk Modulus (B)	Voigt	194.79 GPA	195.20 GPA	0.21%
	Reuss	194.10 GPA	194.40 GPA	0.15%
	Hill	194.45 GPA	194.80 GPA	0.18%
Young's Modulus (E)	Voigt	301.97 GPA	303.10 GPA	0.37%
	Reuss	300.30 GPA	299.90 GPA	−0.13%
	Hill	301.14 GPA	301.50 GPA	0.12%
Shear Modulus (G)	Voigt	121.60 GPA	122.00 GPA	0.33%
	Reuss	120.88 GPA	120.50 GPA	−0.31%
	Hill	121.24 GPA	121.25 GPA	0.01%

Continued

	Voigt	0.24162	0.24200	0.16%
Poisson's Ratio	Reuss	0.24215	0.24150	−0.27%
	Hill	0.24188	0.24175	−0.05%

Table 3. Pugh's ratio.

Averaging scheme	B/G
Voigt	1.602
Reuss	1.606
Hill	1.604

Poisson's ratio, derived from B and G in Table 2, reflects bonding character: smaller Poisson's ratio (0.1 - 0.25) is more covalent-like, whereas larger (0.25 - 0.35) is more ionic-like [18] The ductile or brittle nature of a material can be effectively evaluated using Pugh's ratio (B/G), where values greater than 1.75 indicate ductility, while lower values correspond to brittle behavior (Pugh, 1954). In the present study, the calculated B/G value of approximately 1.60, as indicated in Table 3, lies well below the critical threshold, confirming the intrinsically brittle nature of AlN. This observation is consistent with previous experimental and first-principles investigations, which have reported AlN as a brittle ceramic material with high elastic stiffness and limited plastic deformation capability. Such inherent brittleness has important implications for mechanically active applications, where appropriate structural design and stress management strategies are necessary to ensure long-term reliability. Nevertheless, the high elastic stiffness of AlN enables efficient stress transfer and reversible elastic deformation under small strains, which is advantageous for piezoelectric and thermally driven energy-harvesting applications where cyclic elastic stability is required.

Finally, we note that hardness correlates more strongly with shear modulus (and with elastic/plastic descriptors than with bulk modulus alone. The brittleness of AlN means it can sustain only limited plastic deformation, but its high stiffness and mechanical stability (all Born criteria satisfied) ensure it can reliably endure the small elastic strains involved in energy-harvesting operation.

The elastic anisotropy of hexagonal AlN was evaluated using the Zener anisotropy factor [9]. For a completely isotropic material, the Zener factor equals unity, whereas deviations from unity indicate the degree of elastic anisotropy [19]. In the present study, the calculated anisotropy factor for AlN differs significantly from one, revealing pronounced elastic anisotropy between the basal plane and the crystallographic *c*-axis [14]. This behavior reflects the intrinsic directional dependence of bonding in the wurtzite crystal structure [14].

To describe the macroscopic mechanical behavior of polycrystalline AlN, the bulk and shear moduli were determined using the Voigt-Reuss-Hill (VRH) averaging scheme, which provides a reliable approximation by taking the arithmetic mean of the upper (Voigt) and lower (Reuss) bounds. The resulting Hill-averaged

bulk and shear moduli were subsequently employed to estimate the corresponding Young's modulus and Poisson's ratio of the polycrystalline material [20]. Based on the calculated elastic moduli, AlN exhibits a Young's modulus on the order of several hundred gigapascals, confirming its exceptionally high stiffness [18]. In addition, the obtained Poisson's ratio is approximately 0.25, a value characteristic of materials with predominantly covalent bonding [21]. These mechanical parameters indicate that wurtzite AlN is a very stiff and only moderately compressible ceramic, in excellent agreement with both experimental measurements and previous theoretical studies of III-nitride materials.

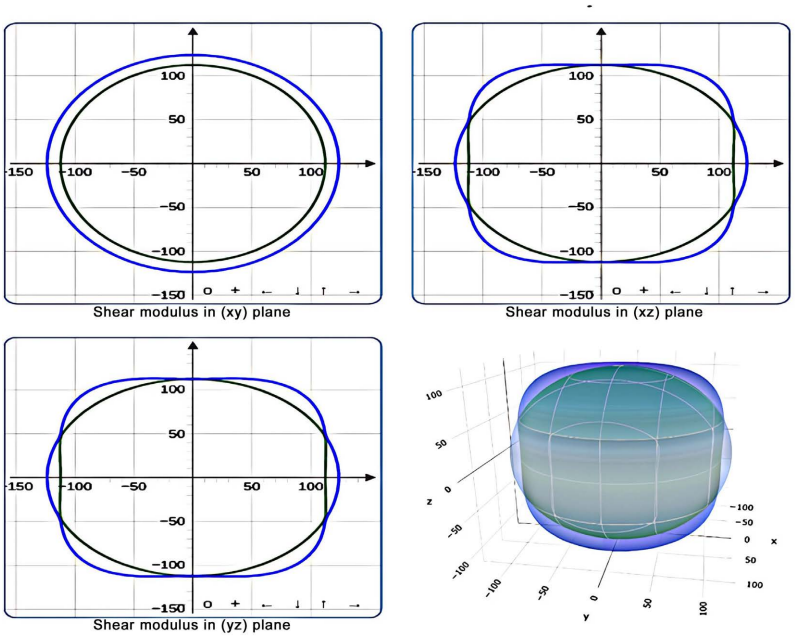

Figure 6. Shear modulus (G) in the in xy, xz, yz plane and 3D.

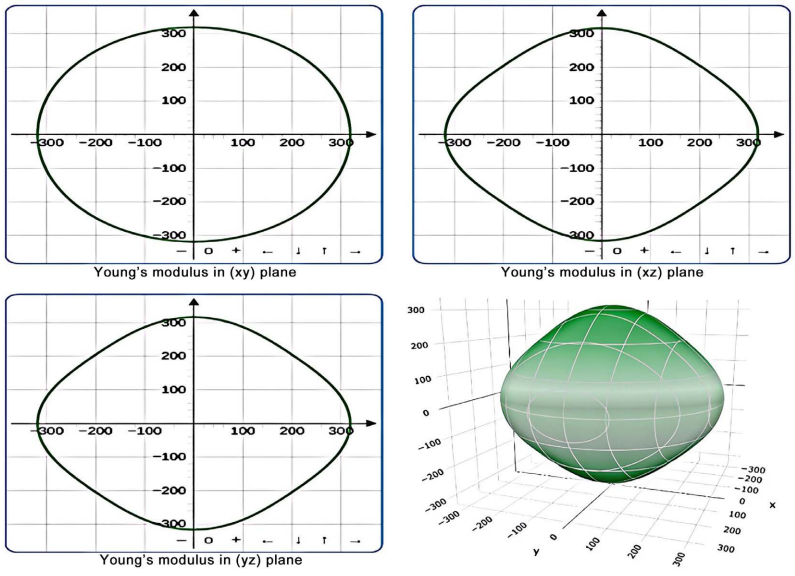

Figure 7. Young's modulus (E) in xy, xz, yz plane and 3D.

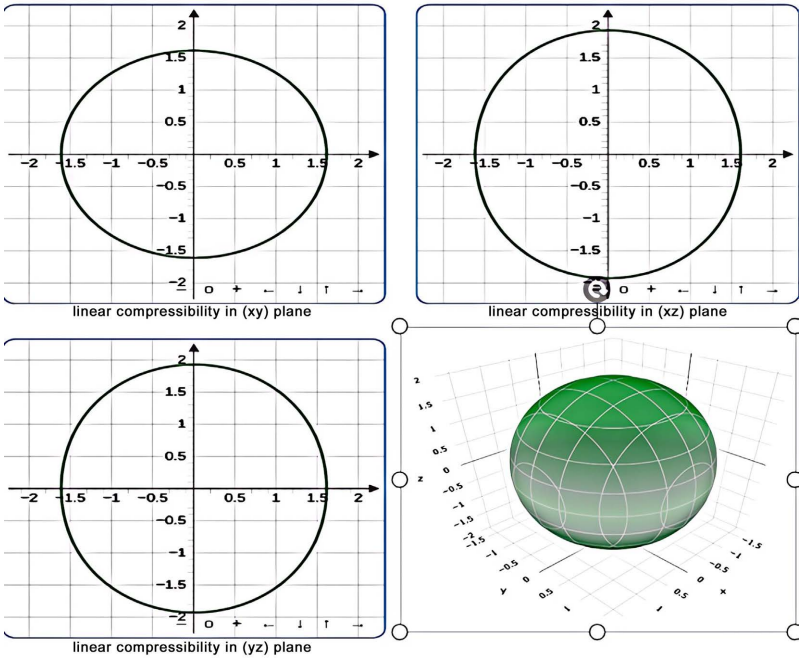

Figure 8. Shear compressibility in the xy, xz, yz plane and 3D.

We visualized the directional dependence of the elastic moduli to further assess anisotropy. **Figure 6**, **Figure 7** and **Figure 8** show stereographic projections (in the yz-plane for clarity) of the shear modulus, Young's modulus, and compressibility, respectively [15]. These plots highlight the anisotropic mechanical response of hexagonal AlN, with stiffness differing along various crystallographic directions. Notably, the c-axis direction exhibits different elastic behavior compared to the basal plane, reflecting the lower crystal symmetry in that direction. Despite the anisotropy, AlN's overall elastic response is dominated by its high stiffness and brittleness, which are advantageous for maintaining structural integrity in piezoelectric devices [22].

The elastic constants we obtained for w-AlN are in good agreement with previously reported values (within a few percent). The slight discrepancies can be attributed to differences in computational method or pseudopotentials used in literature. Our results confirm that wurtzite AlN is mechanically stable and very stiff. The relatively low Poisson's ratio of 0.25 and Pugh's ratio < 1.75 categorize AlN as a brittle material, meaning it will fracture with little plastic deformation. In the context of energy harvesting, this brittleness is not necessarily detrimental; in fact, a rigid, brittle material can sustain repeated elastic cycling strain and release without dissipating much energy through plastic deformation, which is desirable for a piezoelectric generator. The key is that the material must be operated within its elastic regime to avoid fracture (**Figure 9**).

From an energy-harvesting perspective, the elastic properties play a critical role in governing electromechanical coupling, as piezoelectric coefficients are intrinsically linked to both polarization response and elastic compliance. The high elastic stiffness of AlN ensures efficient mechanical-to-electrical energy transfer

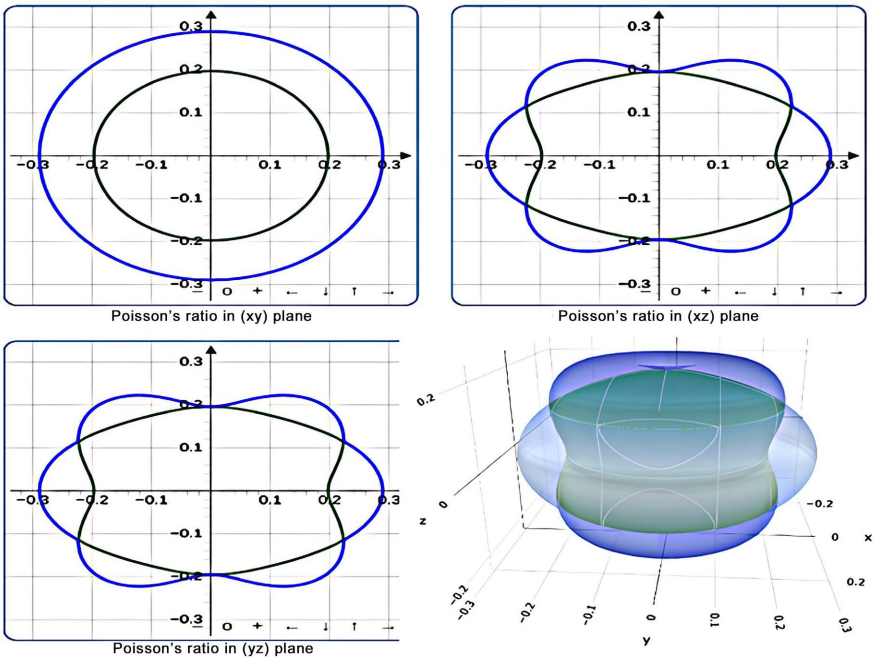

Figure 9. Poisson's ratio in the in xy, xz, yz plane and 3D.

under small applied strains, while its mechanical stability guarantees repeatable operation under cyclic loading. Although the intrinsic brittleness of AlN limits its tolerance to large deformations, its ability to sustain reversible elastic strains without plastic dissipation is advantageous for piezoelectric generator applications, provided that device operation remains within the linear elastic regime. In addition, robust elastic stability is essential for thermoelectric devices operating under temperature gradients, where thermal expansion-induced stresses can degrade performance over time. Therefore, the present elastic and anisotropic mechanical analysis provides an essential foundation for understanding and optimizing both the electromechanical and thermoelectric performance of AlN-based energy-harvesting systems.

3.3. Thermoelectric Properties

The thermoelectric properties of AlN were investigated computationally based on the electronic structure obtained from density functional theory. The transport coefficients were evaluated within the framework of semi-classical Boltzmann transport theory, as implemented through post-processing of the DFT band structure under the constant relaxation time approximation Within this approach, the Seebeck coefficient, electrical conductivity and electronic contribution to thermal conductivity are derived from the energy-dependent band velocities and density of states, enabling temperature-dependent transport trends to be analyzed without requiring explicit scattering calculations [23].

The thermoelectric transport coefficients were obtained by post-processing the converged DFT band structure using the BoltzTraP2 code within the semiclassical Boltzmann transport framework under the constant relaxation time approxima-

tion (CRTA). The calculations were performed for intrinsic (undoped) wurtzite AlN by scanning the chemical potential around the Fermi level; therefore carrier concentrations arise only from thermally excited electrons across the wide band gap. Electrical conductivity is reported in the σ/τ form, since the carrier relaxation time τ is not explicitly calculated. The very small conductivity values therefore reflect the intrinsic ultra-wide-band-gap nature of AlN rather than scattering limitations. The lattice thermal conductivity was not computed from first-principles phonon transport but interpreted based on the known strong covalent bonding and light atomic masses of III-nitride materials, consistent with experimentally reported high thermal conductivity. This methodology explains the combination of moderate Seebeck coefficient, extremely low electrical conductivity, and consequently very small thermoelectric figure of merit (ZT) obtained for wurtzite AlN.

The thermoelectric response of a material is governed by three interrelated quantities: the Seebeck coefficient S (voltage generated per unit temperature difference), the electrical conductivity σ and the thermal conductivity κ (here primarily lattice thermal conductivity, since AlN is an insulator). The interplay of these quantities determines the dimensionless thermoelectric figure of merit, $ZT = S^2\sigma T/\kappa$ [24].

Figure 10 shows the calculated Seebeck coefficient as a function of temperature. The negative sign of S over the investigated temperature range indicates dominant electron-type transport, consistent with the conduction-band characteristics obtained from the DFT electronic structure. The magnitude of S increases with temperature, reflecting enhanced thermal excitation of charge carriers in this wide-band-gap semiconductor. However, a large Seebeck coefficient alone does not guarantee good thermoelectric performance and must be considered together with σ and κ.

The temperature dependence of the thermal conductivity is presented in Figure 11. AlN exhibits a high lattice thermal conductivity due to its strong covalent bonding and light constituent atoms, which permit long phonon mean free paths. With increasing temperature, κ decreases as phonon-phonon Umklapp scattering becomes more significant. Despite this reduction, the thermal conductivity remains relatively large across the examined temperature range, which is unfavorable for thermoelectric energy conversion because it limits the maintenance of temperature gradients.

Figure 12 illustrates the calculated electrical conductivity as a function of temperature. Owing to the ultra-wide band gap of AlN, the intrinsic carrier concentration is extremely low at low temperatures, resulting in very small σ values. As temperature increases, σ rises gradually due to thermal activation of electrons across the band gap, although the increase remains limited by strong phonon scattering at elevated temperatures. Consequently, the electrical conductivity remains orders of magnitude lower than that required for efficient thermoelectric materials.

The combined temperature dependence of S, σ and κ yields the thermoelectric figure of merit shown in Figure 13. Although moderate Seebeck coefficients are

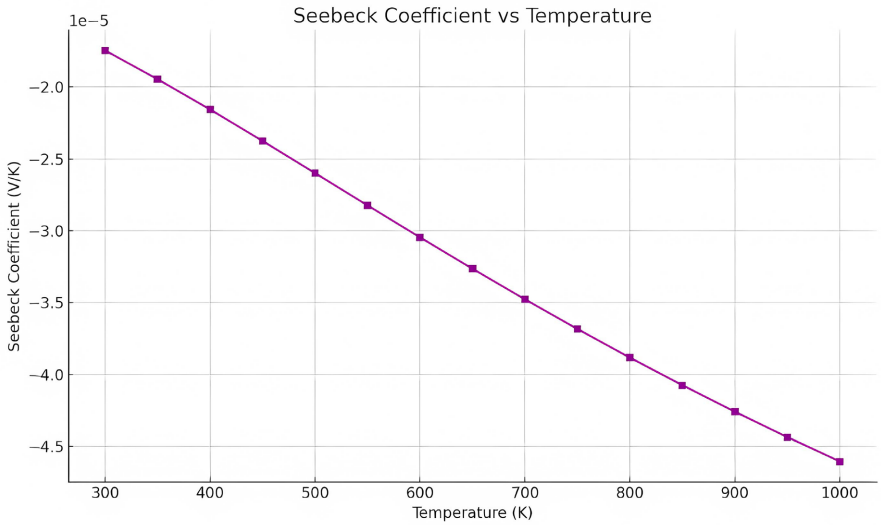

Figure 10. Graph of see-beck coefficient against temperature.

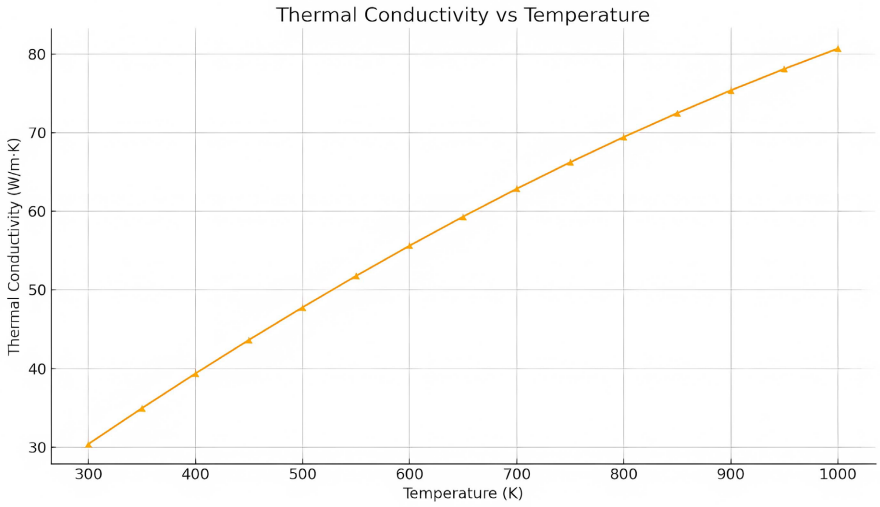

Figure 11. A graph of Thermal conductivity against temperature.

obtained at elevated temperatures, the simultaneously low electrical conductivity and high thermal conductivity result in a very small power factor ($S^2\sigma$) and correspondingly low ZT values across the entire temperature range

The computational results show that pristine AlN exhibits intrinsically poor thermoelectric performance due to its ultra-wide band gap, which suppresses electrical conductivity and its high lattice thermal conductivity, which limits temperature-gradient retention. As a result, the thermoelectric figure of merit remains very low across the investigated temperature range. Nevertheless, these same characteristics provide excellent thermal stability and mechanical robustness, making AlN well suited for piezoelectric energy-harvesting applications. Enhancement of thermoelectric performance in AlN would require controlled doping to increase carrier concentration or alloying strategies, such as AlGaN or Sc-doped AlN, to reduce lattice thermal conductivity while preserving the non-centrosymmetric

wurtzite structure and piezoelectric functionality. Accordingly, compositionally engineered AlN-based systems represent a promising route toward multifunctional energy-harvesting materials.

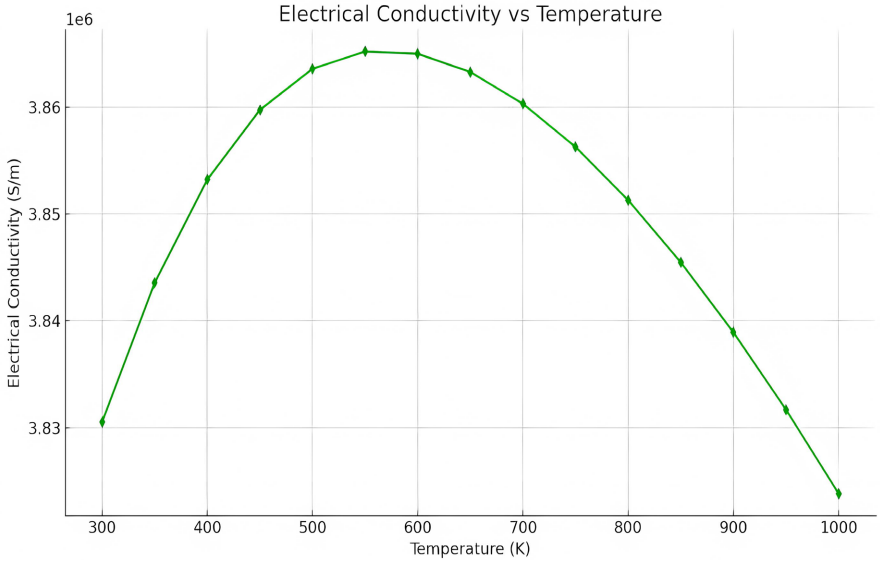

Figure 12. A graph of electrical conductivity against temperature.

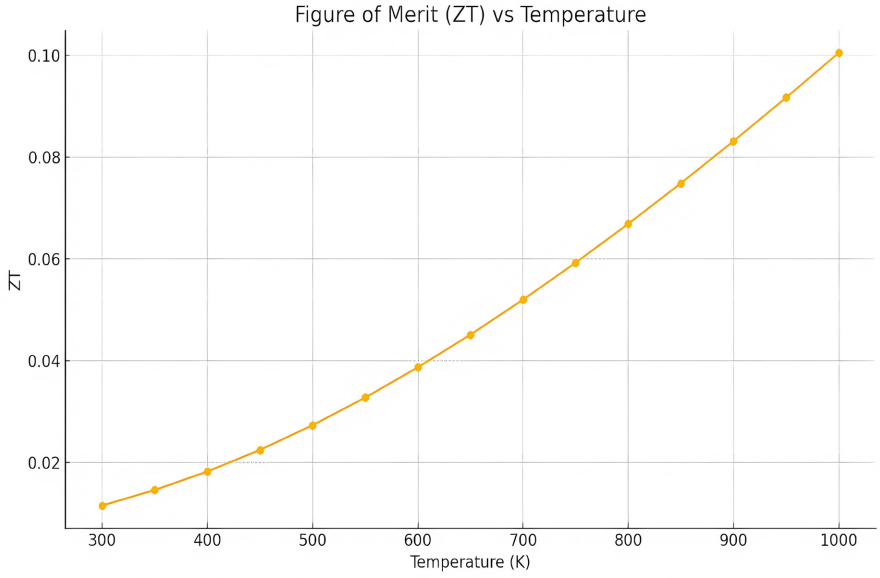

Figure 13. A graph of ZT against temperature.

4. Conclusions

A systematic, convergence-verified first-principles investigation of wurtzite aluminum nitride has been presented, integrating electronic, mechanical and thermoelectric descriptors within a single computational framework. The optimized structural parameters agree closely with experimental data, confirming the reliability of the adopted methodology. Electronic structure calculations establish AlN

as a wide direct-band-gap semiconductor with valence-band states dominated by N-2p orbitals and conduction-band states derived primarily from Al-3s/3p orbitals.

The computed elastic constants satisfy all Born stability criteria for hexagonal crystals and reveal a highly stiff, elastically anisotropic material. Voigt-Reuss-Hill averaged moduli and a Pugh's ratio below 1.75 confirm the intrinsically brittle character of AlN, a feature that limits large plastic deformation but supports efficient elastic energy transfer under cyclic loading. Thermoelectric transport analysis indicates that pristine AlN exhibits very low thermoelectric efficiency due to its ultra-wide band gap and high lattice thermal conductivity, despite moderate Seebeck coefficients at elevated temperatures.

Overall, the results demonstrate that while AlN is not suited for conventional thermoelectric power generation, its mechanical robustness, thermal stability and reliable elastic response make it an excellent lead-free material for piezoelectric energy-harvesting applications. The present work provides a consistent theoretical reference for AlN and offers guidance for future enhancement strategies based on alloying or controlled doping.

Data Availability Statement

The data that support the findings of this study (DFT input files, key output files, and analysis scripts) are available from the corresponding author upon reasonable request.

Acknowledgements

I thank my colleagues for helpful discussions and technical support throughout this work.

Conflicts of Interest

The authors declare that there are no competing interests.

References

[1] Ahmed, B. and Sharma, B.I. (2021) Structural and Electronic Properties of ALN in Rocksalt, Zinc Blende and Wurtzite Phase: A DFT Study. *Digest Journal of Nanomaterials and Biostructures*, **16**, 125-133. https://doi.org/10.15251/djnb.2021.161.125

[2] Jadoon, N.A.K., Puvanenthiram, V., Mosa, M.A.H., Sharma, A. and Wang, K. (2024) Recent Advances in Aluminum Nitride (ALN) Growth by Magnetron Sputtering Techniques and Its Applications. *Inorganics*, **12**, Article 264. https://doi.org/10.3390/inorganics12100264

[3] Soltany-Sadrabadi, A.R. and Aghamir, F.M. (2025) Interaction of a Two-Color Laser with Aluminum Nitride Crystal Leading to THz Radiation. *Applied Physics B*, **131**, Article No. 122. https://doi.org/10.1007/s00340-025-08484-1

[4] Qin, G., Zhao, Z., Wang, A., Wang, W., Qin, S., Wu, H., *et al.* (2024) Investigation of Piezoelectric Properties of Wurtzite AlN Films under In-Plane Strain: A First-Principles Study. *Coatings*, **14**, 984. https://doi.org/10.3390/coatings14080984

[5] Çipiloğlu, M.A. and Özkurt, A. (2020) Theoretical Investigation on Molecular Structure and Electronic Properties of B_xLi_y Cluster for Lithium-Ion Batteries with Quantum ESPRESSO Program. *Molecules*, **25**, 3266. https://doi.org/10.3390/molecules25143266

[6] Aborah Yeboah, L., Abdul Malik, A., Agyemang Oppong, P., Sarfo Acheampong, P., Arko Morgan, J., Akua Adwubi Addo, R., *et al.* (2025) Wide-Bandgap Semiconductors: A Critical Analysis of GaN, SiC, AlGaN, Diamond, and Ga_2O_3 Synthesis Methods, Challenges, and Prospective Technological Innovations. *Intelligent and Sustainable Manufacturing*, **2**, 10011-10011. https://doi.org/10.70322/ism.2025.10011

[7] Zhu, L., Zhang, X., Hou, Q., Lu, Y., Keal, T.W., Buckeridge, J., *et al.* (2024) Formation of Intrinsic Point Defects in AlN: A Study of Donor and Acceptor Characteristics Using Hybrid QM/MM Techniques. *Journal of Materials Chemistry A*, **12**, 25449-25464. https://doi.org/10.1039/d4ta04335a

[8] Escorcia-Salas, G.E., Restrepo-Leal, D., Martinez-Castro, O., López-Pérez, W. and Sierra-Ortega, J. (2023) Structural, Electronic, and Optical Properties of Wurtzite $V_xAl_{1-x}N$ Alloys: A First-Principles Study. *Condensed Matter*, **8**, Article 61. https://doi.org/10.3390/condmat8030061

[9] Li, G., Zhu, M., Guo, Z., Yang, Y., Li, H., Shang, J., *et al.* (2024) Recent Advances in III-V Nitrides: Properties, Applications and Perspectives. *Journal of Materials Chemistry C*, **12**, 12150-12178. https://doi.org/10.1039/d4tc02615b

[10] Mouhat, F. and Coudert, F. (2014) Necessary and Sufficient Elastic Stability Conditions in Various Crystal Systems. *Physical Review B*, **90**, Article ID: 224104. https://doi.org/10.1103/physrevb.90.224104

[11] Ech-chaachoui, Z., Ait Cheikh, K., Khalfi, H., Naciri, I., Yu, J., Elmaimouni, L., *et al.* (2025) Vibration Characteristics of Piezoelectric Annular Plates with Annular Metallization: An Extended Polynomial Method. *Mechanics of Advanced Materials and Structures*. https://doi.org/10.1080/15376494.2025.2541062

[12] Yin, H. and Liu, C. (2023) Anisotropy and Asymmetry of the Elastic Tensor of Lattice Materials. *Journal of Elasticity*, **154**, 659-691. https://doi.org/10.1007/s10659-023-10028-7

[13] Golesorkhtabar, R., Pavone, P., Spitaler, J., Puschnig, P. and Draxl, C. (2013) Elastic: A Tool for Calculating Second-Order Elastic Constants from First Principles. *Computer Physics Communications*, **184**, 1861-1873. https://doi.org/10.1016/j.cpc.2013.03.010

[14] Ez-zejjari, I., Ghazi, H.E., Belaid, W., En-nadir, R., Abboudi, H. and Sali, A. (2025) Hydrostatic-Pressure Modulation of Band Structure and Elastic Anisotropy in Wurtzite BN, AlN, GaN and InN: A First-Principles DFT Study. *Crystals*, **15**, Article 648. https://doi.org/10.3390/cryst15070648

[15] Born, M. and Huang, K. (1954) Dynamical Theory of Crystal Lattices. Oxford University Press.

[16] Kürkçü, C. and Yamçıçıer, Ç. (2025) The Investigation of Structural, Elastic, Electronic, Vibrational, Thermo-Physical, and Optical Properties of Hexagonal-Type X_2N (X = Mn, Tc, and Re) Compounds. *Indian Journal of Physics*, **99**, 4565-4583. https://doi.org/10.1007/s12648-025-03663-4

[17] Baaziz, H., Ghellab, T., Charifi, Z., Güler, M., Uğur, Ş., Güler, E., *et al.* (2023) Full Potential Theoretical Investigations for Electronic, Optical, Mechanical, Elastic and Anisotropic Properties of X_2Se_2C (X = Ta, Nb) Compounds. *The European Physical Journal B*, **96**, Article No. 55. https://doi.org/10.1140/epjb/s10051-023-00526-x

[18] Shao, H., Wang, Y., Song, J., Lei, L., Liu, X., Hou, X., *et al.* (2025) First-Principles

Calculation of Mechanical Properties and Thermal Conductivity of C-Doped AlN. *Ceramics*, **8**, Article 117. https://doi.org/10.3390/ceramics8030117

[19] Petrazoller, J., Guénolé, J., Berbenni, S. and Richeton, T. (2025) On the Effect of Elastic Anisotropy and Polarizability on Solute Segregation at Low-Angle Grain Boundaries. *Computational Materials Science*, **249**, Article ID: 113642. https://doi.org/10.1016/j.commatsci.2024.113642

[20] Li, L., Yan, X., Yang, B., Yang, S., Volinsky, A.A. and Pang, X. (2023) First-Principles Calculations of the AlN/Ti Interface Properties. *Chemical Physics Letters*, **826**, Article ID: 140649. https://doi.org/10.1016/j.cplett.2023.140649

[21] Neupane, H.K., Oli, D., Rijal, O.S., Neupane, R.K., Shrestha, P., Sharma, S., *et al.* (2025) Exploring the Structural, Dynamical, Mechanical, Electronic, Magnetic, and Optical Properties of Ta_2AlN, Ti_2AlN & Ti_2GaN MAX Phase Compounds: First-Principles Study. *Heliyon*, **11**, e42962. https://doi.org/10.1016/j.heliyon.2025.e42962

[22] Jung, Y., Lee, D. and Kim, J. (2025) Recent Progress in Aluminum Nitride for Piezoelectric MEMS Mirror Applications: Enhancements with Scandium Doping. *Microsystems & Nanoengineering*, **11**, Article No. 179. https://doi.org/10.1038/s41378-025-01053-8

[23] Neophytou, N., Priyadarshi, P., Li, Z. and Graziosi, P. (2023) Electronic Transport Computation in Thermoelectric Materials: From *Ab Initio* Scattering Rates to Nanostructures. *Journal of Computational Electronics*, **22**, 1264-1280. https://doi.org/10.1007/s10825-023-02075-z

[24] Hasan, S., San, S., Baral, K., Li, N., Rulis, P. and Ching, W. (2022) First-Principles Calculations of Thermoelectric Transport Properties of Quaternary and Ternary Bulk Chalcogenide Crystals. *Materials*, **15**, Article 2843. https://doi.org/10.3390/ma15082843